



香港城市大學  
City University of Hong Kong

專業 創新 胸懷全球  
Professional · Creative  
For The World

## CityU Scholars

### Restoring the silenced surface second-harmonic generation in split-ring resonators by magnetic and electric mode matching

Liu, Shao-Ding; Yue, Peng; Zhu, Ming-Qi; Wen, Jing; Lei, Danguan

**Published in:**  
Optics Express

**Published:** 16/09/2019

**Document Version:**  
Final Published version, also known as Publisher's PDF, Publisher's Final version or Version of Record

**Publication record in CityU Scholars:**  
[Go to record](#)

**Published version (DOI):**  
[10.1364/OE.27.026377](https://doi.org/10.1364/OE.27.026377)

**Publication details:**  
Liu, S-D., Yue, P., Zhu, M-Q., Wen, J., & Lei, D. (2019). Restoring the silenced surface second-harmonic generation in split-ring resonators by magnetic and electric mode matching. *Optics Express*, 27(19), 26377-26391. <https://doi.org/10.1364/OE.27.026377>

#### **Citing this paper**

Please note that where the full-text provided on CityU Scholars is the Post-print version (also known as Accepted Author Manuscript, Peer-reviewed or Author Final version), it may differ from the Final Published version. When citing, ensure that you check and use the publisher's definitive version for pagination and other details.

#### **General rights**

Copyright for the publications made accessible via the CityU Scholars portal is retained by the author(s) and/or other copyright owners and it is a condition of accessing these publications that users recognise and abide by the legal requirements associated with these rights. Users may not further distribute the material or use it for any profit-making activity or commercial gain.

#### **Publisher permission**



Permission for previously published items are in accordance with publisher's copyright policies sourced from the SHERPA RoMEO database. Links to full text versions (either Published or Post-print) are only available if corresponding publishers allow open access.

#### **Take down policy**

Contact [lbscholars@cityu.edu.hk](mailto:lbscholars@cityu.edu.hk) if you believe that this document breaches copyright and provide us with details. We will remove access to the work immediately and investigate your claim.



# Restoring the silenced surface second-harmonic generation in split-ring resonators by magnetic and electric mode matching

SHAO-DING LIU,<sup>1,5</sup>  PENG YUE,<sup>1</sup> MING-QI ZHU,<sup>1</sup> JING WEN,<sup>2</sup>   
AND DANGYUAN LEI<sup>3,4</sup> 

<sup>1</sup>Key Lab of Advanced Transducers and Intelligent Control System of Ministry of Education, and Department of Physics and Optoelectronics, Taiyuan University of Technology, Taiyuan 030024, China

<sup>2</sup>Engineering Research Centre of Optical Instruments and Systems, Ministry of Education and Shanghai Key Lab of Modern Optical Systems, University of Shanghai for Science and Technology, Shanghai 200093, China

<sup>3</sup>Department of Materials Science and Engineering, City University of Hong Kong, 83 Tat Chee Avenue, Kowloon, Hong Kong, China

<sup>4</sup>dangylei@cityu.edu.hk

<sup>5</sup>liushaoding@tyut.edu.cn

**Abstract:** Surface second-harmonic generation (SHG) in plasmonic metal nanostructures provides a promising approach to design compact and ultrafast nonlinear nanophotonics devices. However, typical plasmonic nanostructures, such as those with tiny gaps that provide strong near-field-amplified nonlinear sources, often suffer from the cancellation of nonlinear fields in the gaps, which results in the so-called silenced SHG and consequently attenuates the overall nonlinear conversion efficiency. In this study, we propose and demonstrate that the silenced SHG in a gold split-ring resonator can be effectively restored by carefully tailoring its gap geometry to avoid the cancellation of nonlinear fields in the gap and simultaneously achieve both spatial and frequency mode matching between the magnetic and the electric dipolar resonances. As a result, the effective nonlinear sources in the gap can be dramatically amplified and the surface second-harmonic emissions can be efficiently coupled out, leading to an SHG intensity enhancement of 7 times compared to a conventional split-ring resonator. The overall SHG conversion efficiency can thus be enlarged to about  $1.49 \times 10^{-8}$  in the near-infrared excitation region. Importantly, the restored surface second-harmonic emission exhibits the scattering characteristics of an ideal electric dipole, which can be very useful for nonlinear far-field manipulation such as beam steering and holograms.

© 2019 Optical Society of America under the terms of the [OSA Open Access Publishing Agreement](#)

## 1. Introduction

Surface second-harmonic generation (SHG) in plasmonic metal nanostructures plays an important role in modern nonlinear nanophotonics devices [1–9]. Although the nonlinear conversion efficiencies are in general weaker than that of their dielectric counterparts [10], plasmonic nanostructures possess superior performance in many aspects benefiting from their extraordinary surface sensitivities and tiny mode volumes. For example, plasmonic SHG nanostructures have been widely studied in the context of nonlinear biosensing [11–14], single nanoparticle mapping [15], and nonlinear far-field manipulation [16–24]. Besides that, numerous strategies have been developed to enhance the surface SHG efficiencies in plasmonic nanostructures, including symmetry breaking [25,26], surface lattice modes [27–29], Fano resonances [30–33], index-matching antennas [34,35], and hybridized nanoparticles [36–40].

It is well known that the strength of SHG nonlinear sources is proportional to the field intensity at the fundamental wavelength, and therefore plasmonic nanostructures with tiny gaps are often used to enhance the nonlinear conversion efficiency. However, the so-called silenced SHG that strongly attenuates the emission intensity has been observed in plasmonic nano-rod dimers [41,42]. It is shown that, although there is a stronger near-field enhancement around the resonance, the SHG emission intensity decreases significantly when the incidence frequency is approaching to the resonance of the system. This phenomenon is caused by the cancelation of nonlinear fields in the gap region [41,42]. Similar results have been observed with asymmetric nanorod dimers [43], dense arranged clusters under cylindrical vector beam excitation [44], and nanodisks with tiny splits [45]. The silenced SHG can be restored by using electrically-connected antennas [41], lowering structural symmetry [46], or adjusting gap positions to form double resonant antennas [47]. Nevertheless, the SH emissions in these structures are often amplified by higher-order plasmon resonances, whose scattering efficiencies are inherently weaker than that of dipolar resonances [48–50].

Among the above-mentioned plasmonic nanostructures, metallic split-ring resonators (SRRs) are a promising class of structures for realizing enhanced SHG [51], where the nonlinear sources at the fundamental excitation wavelength can be enhanced with its magnetic dipolar (MD) resonance mode and the nonlinear emission scattering at the SH wavelength amplified by its electric dipolar (ED) resonance mode. As a result, the nonlinear far-field radiation features the scattering characteristics of the ED mode [52–54]. Since the SRR SHG is governed by the nonlinear sources generated in the gap region, the cancelation of nonlinear fields may significantly attenuate the SHG emission of the system when the fundamental excitation wavelength matches the MD resonance band. In order to overcome this issue, we propose and demonstrate that the silenced SHG can be effectively restored by delicately engineering the SRR gap geometry to avoid the cancellation of nonlinear fields and also achieve both spatial and frequency mode matching of the MD and ED resonances.

## 2. Silenced SHG in conventional SRRs

The inset of Fig. 1(a) sketches a conventional SRR with a rectangular gap, the scattering (absorption) spectrum of which under  $x$ -polarized incidence exhibits a strong resonance at around 900 nm with a larger scattering efficiency than the absorption efficiency, where the outer radius  $R$ , the inner radius  $r$  and the thickness of the SRRs are 80, 40, and 30 nm, respectively. The multipolar expansion results in Fig. 1(a) reveal that the ED contribution of this resonance plays a dominant role in the scattering cross-section, indicating its ED nature. This is consistent with the simulated near-field distribution at the resonance position which features two relatively strong near-field lobes around the SRR (see the left panel of Fig. 1(d)), forming an equivalent ED oriented along the  $x$ -axis. As a result, both the three-dimensional far-field radiation pattern and its two-dimensional polar plot exhibit the scattering characteristics of the ED mode (see the middle panel of Fig. 1(d)), i.e. a typical doughnut shape with the same radiation intensity distribution profile in the  $x$ - $y$  and  $x$ - $z$  planes (see the right panel of Fig. 1(d)).

Under  $y$ -polarized incidence, the scattering and absorption spectra of the SRR in Fig. 1(b) exhibit a pronounced resonance at around 1800 nm yet with a weaker scattering efficiency than the absorption efficiency, indicating an effectively suppressed radiative damping. The multipolar expansion results show that, in addition to the dominant ED component (the green dashed line), the MD component is significantly leveraged, indicating excitation of the so-called MD mode of the SRR. This is also consistent with the simulated near-field distribution where the fields are tightly localized in the gap region (see the left panel of Fig. 1(e)), resulting in an overall equivalent ED dipole along the incidence polarization. Importantly, the rotating near-field currents in the ring lead to the formation of an equivalent MD oriented along the  $z$ -axis [51–54]. Due to spatial overlapping of the ED and MD modes, the far-field radiation pattern at this resonance dramatically

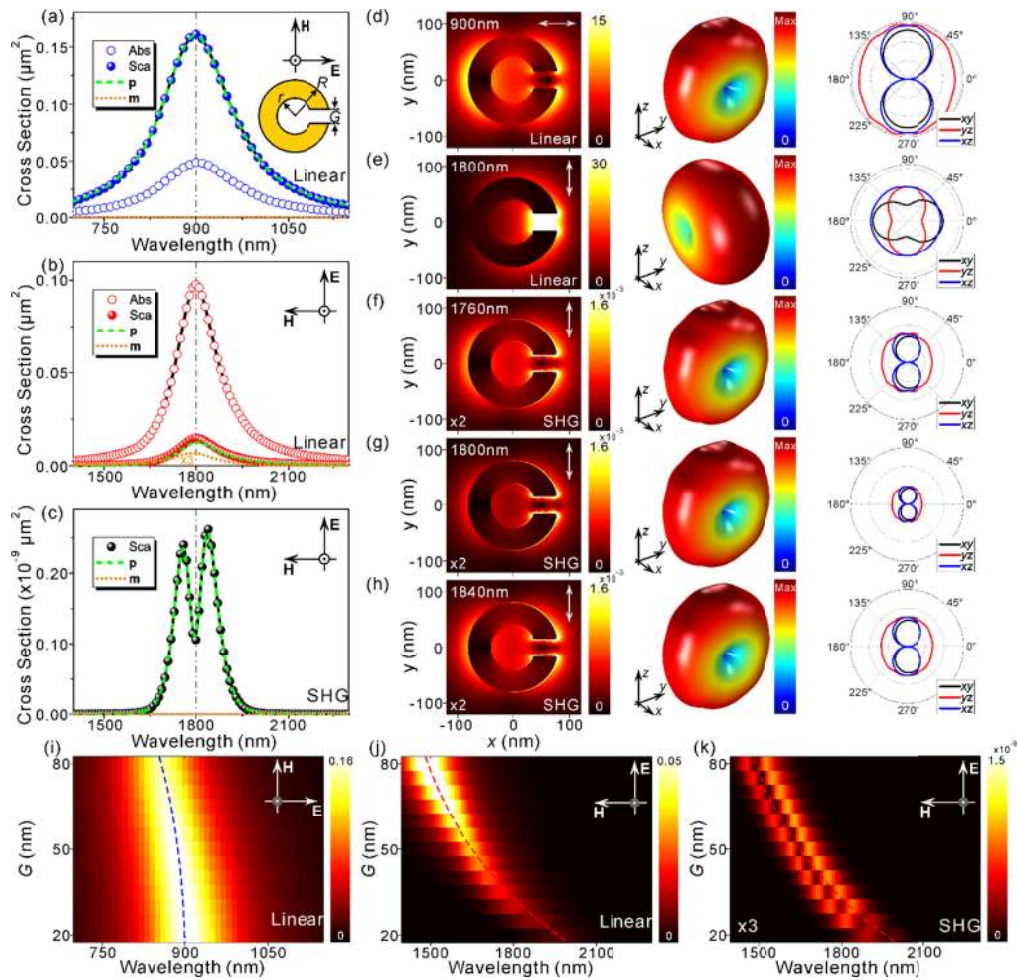


**Fig. 1.** SHG in conventional SRRs of a rectangular gap, with an outer radius  $R = 80$  nm and an inner radius  $r = 40$  nm. The thickness of each SRR is  $30$  nm, and  $G$  in the inset of (a) denotes the SRR gap width. (a, b) Scattering (solid circular points) and absorption (open circular points) spectra for an SRR with  $G = 30$  nm under (a)  $x$ - and (b)  $y$ -polarized incidence. The green dashed and the orange dotted lines represent, respectively, the electric dipole ( $\mathbf{p}$ ) and the magnetic dipole ( $\mathbf{m}$ ) contributions obtained from multipolar decomposition of the scattering spectra. The  $\mathbf{m}$  contribution is scaled by a factor of 3 for better visualization. The corners of the SRR structure are rounded by  $3$  nm to avoid unphysical singularities. (c) SHG scattering spectrum under  $y$ -polarized incidence. (d-h) Electric near-field amplitude distribution profiles (the left panels), three-dimensional far-field radiation patterns (the middle panels), and cross-sectional views of far-field scattering patterns under  $x$ -polarized incidence at  $\lambda_{\text{inc}} = 900$  nm (d), under  $y$ -polarized incidence at  $\lambda_{\text{inc}} = 1800$  nm (e), and SHG electric near-field amplitude distribution profiles under  $y$ -polarized incidence at  $\lambda_{\text{inc}} = 1760$  nm (f),  $1800$  nm (g), and  $1840$  nm (h). The SHG near-field amplitudes in (f-g) are scaled by a factor of 2. (i-k) Fundamental (i, j) and SH (k) scattering cross-sections as functions of gap width  $G$  and incident wavelength under  $x$ - (i) and  $y$ -polarized (j, k) incidence. The SH scattering cross sections in (k) are scaled by a factor of 3. The blue and the red dashed lines denote the spectral positions of the ED and the MD modes, respectively.

differs from that of an ideal dipole scattering (see the middle panel of Fig. 1(e)), manifested itself by totally different distribution profiles in the three planes (see the right panel of Fig. 1(e)).

Since the ED resonance mode in Fig. 1(a) is at the SH wavelength of the MD mode in Fig. 1(b), the spectral mode-matching condition for efficient SHG is fulfilled in the SRR system, where the nonlinear source can be enhanced in the gap region by the MD mode at the fundamental wavelength and the nonlinear scattering efficiency can be amplified by the ED mode at the SH wavelength. One may expect that the SHG intensity would be the strongest when the incidence frequency matches the MD mode at which the field intensity in the gap region is the largest (see Fig. 5 in the Appendix section). However, the SHG scattering spectrum in Fig. 1(c) reveals that, instead of having a scattering peak, a scattering dip at 1800 nm (accompanied by two scattering peaks at 1760 and 1840nm) appears when the incidence frequency matches the MD mode, where a plane wave with an electric field amplitude of  $1 \times 10^7$  V/m, polarized along the  $y$ -axis and propagating along the  $z$ -axis, is used as the pump beam. This unexpected result indicates the silenced SHG effect in the SRR gap attenuates the SHG emission intensity. Indeed, the simulated SHG near-field distribution profiles in the left panels of Figs. 1(f) – 1(h) demonstrate that the nonlinear fields in the gap region are much weaker at the MD resonance excitation (i.e. at 1800 nm) than that at the two adjacent scattering peaks (i.e. at 1760 and 1840nm). In addition, the multipolar decomposition results of the SHG scattering spectrum reveal that the SHG radiation is dominated by an ED component (see the dashed line in Fig. 1(c)), which is consistent with the far-field scattering patterns shown in the middle and right panels of Figs. 1(f) – 1(h). The SHG scattering of the plasmonic SRR is similar as that of metal nanodisks with tiny splits [45], where the silenced SHG can also be observed in the measured spectrum when the fundamental excitation energy matches with the MD mode resonance.

To better depict the dependence of SHG efficiency on the gap width of a conventional SRR, we calculated the linear and nonlinear scattering cross-sections of the system as functions of gap width and incidence wavelength under  $x$ - and  $y$ -polarized incidence, respectively. The linear results that the ED resonance frequency red shifts slightly with decreasing the gap width (see the blue dashed line in Fig. 1(i)), whereas the MD resonance frequency red shifts rapidly (see the red dashed line in Fig. 1(j)). Besides, the near-field enhancement factor at the fundamental wavelength (corresponding to the nonlinear source strength in the gap) can be enlarged by reducing the gap width (e.g.,  $G = 20$  nm in Figs. 6 and 7). However, the SHG scattering results reveal a pronounced SHG silencing response exactly at the MD resonance frequencies (see the red dashed line in Fig. 1(k)). It is worth to note that, despite the silenced SHG effect, plasmonic SRRs are still a promising class of SHG platforms. For example, the maximum SHG scattering cross-section can be as large as  $2.62 \times 10^{-10} \mu\text{m}^2$  for the SRR with  $G = 30$  nm, and the maximum SHG conversion efficiency is about  $2.90 \times 10^{-9}$  (which is defined as the ratio between the SHG scattering cross section and the linear extinction cross section at the incidence). This value is comparable to that of an L-shaped mode-matching antenna ( $6.4 \times 10^{-9}$ ) [35]. More importantly, the SHG radiation of the SRR preserves the scattering characteristics of an ideal ED resonance mode, enabling straightforward nonlinear far-field manipulation [48–50]. Owing to these unique merits, it is therefore desirable to further leverage the overall SHG conversion efficiency of SRRs by restoring the silenced SHG and coupling out its radiation.

### 3. Physical mechanisms for SHG in conventional and tailored plasmonic SRRs

In the following, the SHG mechanism in conventional SRRs is investigated (Fig. 2(a)), which provides a clue to restore the silenced SHG. The excitation of the MD mode leads to strong near-field enhancements around the gap area, consequently resulting in amplified nonlinear sources for SHG (Scheme I, Fig. 2(a)). Previous studies have shown that SHG with plasmonic nanostructures can be mainly attributed to the surface contribution [55–58]. There are three non-zero surface nonlinear susceptibilities ( $\chi_{\perp\perp\perp}^{(2)}$ ,  $\chi_{\perp\parallel\parallel}^{(2)}$ , and  $\chi_{\parallel\parallel\perp}^{(2)}$ , where  $\perp$  and  $\parallel$  represent the

orientations perpendicular and parallel to the surface of a structure, respectively), among which  $\chi_{\perp\perp\perp\perp}^{(2)}$  plays the dominant role [52,53]. As a result, the generated nonlinear sources can be treated as various equivalent dipoles that perpendicular to the surfaces (Scheme II, Fig. 2(a)), which are mainly accumulated around the gap area. Due to the structural symmetry, the nonlinear sources on the upper and lower surfaces of the gap have the same intensity but with opposite orientations, thereby leading to the cancelation of the nonlinear fields, and the effective nonlinear sources are attenuated significantly (Scheme III, Fig. 2(a)), which is the reason for the silenced SHG. The cancelation of the nonlinear fields leads to the SHG scattering dip when the incidence matches with the MD mode, and the field intensities within the gaps are weak for the SHG near-field distributions (the left panels, Figs. 1(f) – 1(h)). In addition, when the gap is very narrow (*e.g.*,  $G = 20$  nm), the cancelation of nonlinear fields can be more effective, thereby leading to the decreasing of SHG emission (Fig. 1(k)). Nevertheless, the ED mode still can be excited with the residual nonlinear sources (Scheme IV, Fig. 2(a)), which leads to an equivalent electric dipole moment for SHG scattering ( $\mathbf{P}_{\text{SHG}}$ ), and the far-field distributions represent an ideal ED scattering characteristic. It has been demonstrated that SHG calculations using this model agree well with the experimental results, and it is valid even for plasmonic nanoparticles with dimensions much less than the SHG and incident wavelengths [55–58]. Nevertheless, only the surface nonlinear contributions are considered in this model, and the electron pressure term in the bulk region for SHG should be considered when strong field gradients are generated inside the nanoparticles [1].

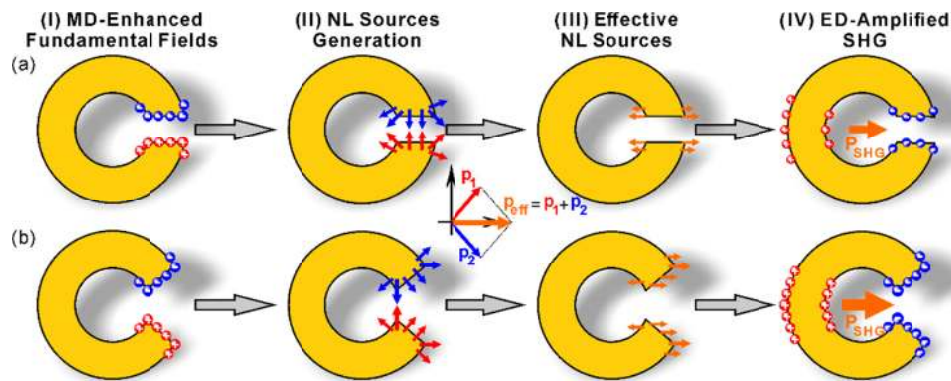


**Fig. 2.** Schematics of silenced SHG in a conventional SRR (a) and restoring the silenced SHG in the SRR of a V-shaped gap (b). (I): Surface charge distribution associated with the MD mode at the fundamental wavelength; (II) Overall and (III) effective nonlinear source distributions in the gap region; and (IV) Surface charge distribution associated with the ED mode at the SH wavelength.

Previous studies have shown that plasmonic SHG is very sensitive to structural geometries. Even though the linear responses are not changed, the SHG far-field scattering patterns change dramatically by slightly modifying plasmonic nanostructure shapes, which is promising for the sensitive optical characterization of nanostructures [15]. Since the SHG nonlinear sources are mainly accumulated around the tiny gap region, carefully tailoring the gap geometry for the SRRs is critical to restore the silenced SHG. From another point of view, the MD and ED modes spectrally overlap with each other for SHG. However, the spatial overlap of the localized fields at the fundamental and the SH wavelengths is poor for the conventional SRRs, where it is found that there are strong localized fields within the gap area for the MD mode (Fig. 1(e)), whereas the fields are very weak for the ED mode (Fig. 1(d)). As a result, most of the nonlinear sources are cancelled with each other, which contribute little to the excitation of the ED mode for SHG, and the nonlinear scattering intensity is attenuated. Noted that the generated effective

nonlinear sources can be seen as a result of the vector superposition of the nonlinear dipoles on the upper and lower surfaces, so the simplest way to enhance the effective source intensity is by adjusting the relative angle between the two gap surfaces (Fig. 2(b)). In this way, the MD mode still can be excited to enhance the nonlinear sources (Scheme I, Fig. 2(b)), which are also oriented perpendicular to the surfaces (Scheme II, Fig. 2(b)). Although the  $y$ -components of the nonlinear sources are cancelling with each other, strong effective nonlinear sources that oriented perpendicular to the polarization can be generated (Scheme III, Fig. 2(b)), and the ED mode would be strongly excited to amplify the SHG (Scheme IV, Fig. 2(b)).

#### 4. Shedding light on silenced SHG by tailoring the SRR gap

To verify the above assumption, the optical responses of the modified SRRs are investigated. The inset of Fig. 3(a) shows the schematic view of the structure, where  $\theta$  and  $s$  denote the angle and the distance of the gap, respectively. When the polarization is along the  $x$ -axis, the solid (open) green points in Fig. 3(a) demonstrate the scattering (absorption) spectrum of the modified SRR with  $s = 20$  nm and  $\theta = 65^\circ$ , and the gray points show the corresponding spectra of the unmodified conventional SRR with  $G = 20$  nm. There is a broad resonance for the modified SRR, and the multipolar expansion results (the dashed and the dotted lines, Fig. 3(a)) and field distributions (Fig. 3(d)) reveal the excitation of the ED mode, where it shifts to the blue side compared with that of the conventional SRR due to the enlarged restoring force.

When the polarization is along the  $y$ -axis (Fig. 3(b)), the resonance of the modified SRR (the red points) blue shifts significantly compared with that of the conventional SRR (the gray points). The multipolar expansions reveal that a MD component is involved in the resonance (the dotted line, Fig. 3(b)). There are also strong near-field enhancements around the gap area (the left panel, Fig. 3(e)), and the far-field scattering patterns are the superposition of the ED and the MD contributions (the middle and the right panels, Fig. 3(e)). Nevertheless, the near-field distributions for the MD and the ED modes are modified along with the geometry changes, which have a direct consequence on nonlinear responses. For example, the generated nonlinear sources around the apexes may cancel each other caused by the structural symmetry, but the relative strong near-field enhancements around the surfaces that away from the apexes lead to enhanced effective nonlinear sources, and the silenced SHG can be restored for the modified SRRs.

The nonlinear spectrum shown in Fig. 3(c) indeed reveals that the SHG scattering is strongly amplified compared with that of the conventional SRRs. The maximum SHG scattering cross section is about  $9.09 \times 10^{-10} \mu\text{m}^2$ , which is more than seven times as large as that of the conventional SRR (the gray points, Fig. 3(c)). Besides that, the maximum conversion efficiency is enlarged to about  $8.00 \times 10^{-9}$ , and the SHG near-fields are also strongly enhanced for the modified SRR (the left panels, Figs. 3(f) – 3(h)). Since the structural symmetry is not changed, the SHG far-field scattering patterns are the same as that of the conventional SRRs, and the ideal ED scattering characteristic is maintained (the middle and the right panels, Figs. 3(f) – 3(h)). It is worth to mention that when the incidence matches the MD mode, a scattering dip appears in the spectrum (Fig. 3(c)), and the silenced SHG still exists for the modified SRR caused by the cancelation of the nonlinear fields around the apexes. Nevertheless, the SHG scattering intensity of the dip is several times larger than that of the conventional SRR, and the intensity ratio between the scattering dip and the maximum scattering peak is enlarged to 54.7% (Fig. 3c), while the ratio is only 40.1% for the conventional SRR (Fig. 1(c)). This indicates the silenced SHG is restored with the modified SRR. Please note that the near-field enhancement associated with the MD mode is strongly amplified in the modified SRR (Fig. 3(e)). In addition to the LSPR enhancement, it can be partially attributed to the lightning rod effect, that is, strong local fields produced by sharp metal tips [59]. Consequently, enhanced nonlinear sources are generated around the gap region, which can also be used to leverage the SHG efficiency. Since all the near-fields around the SRR are used to calculate the nonlinear sources with the hydrodynamic model, the near-field

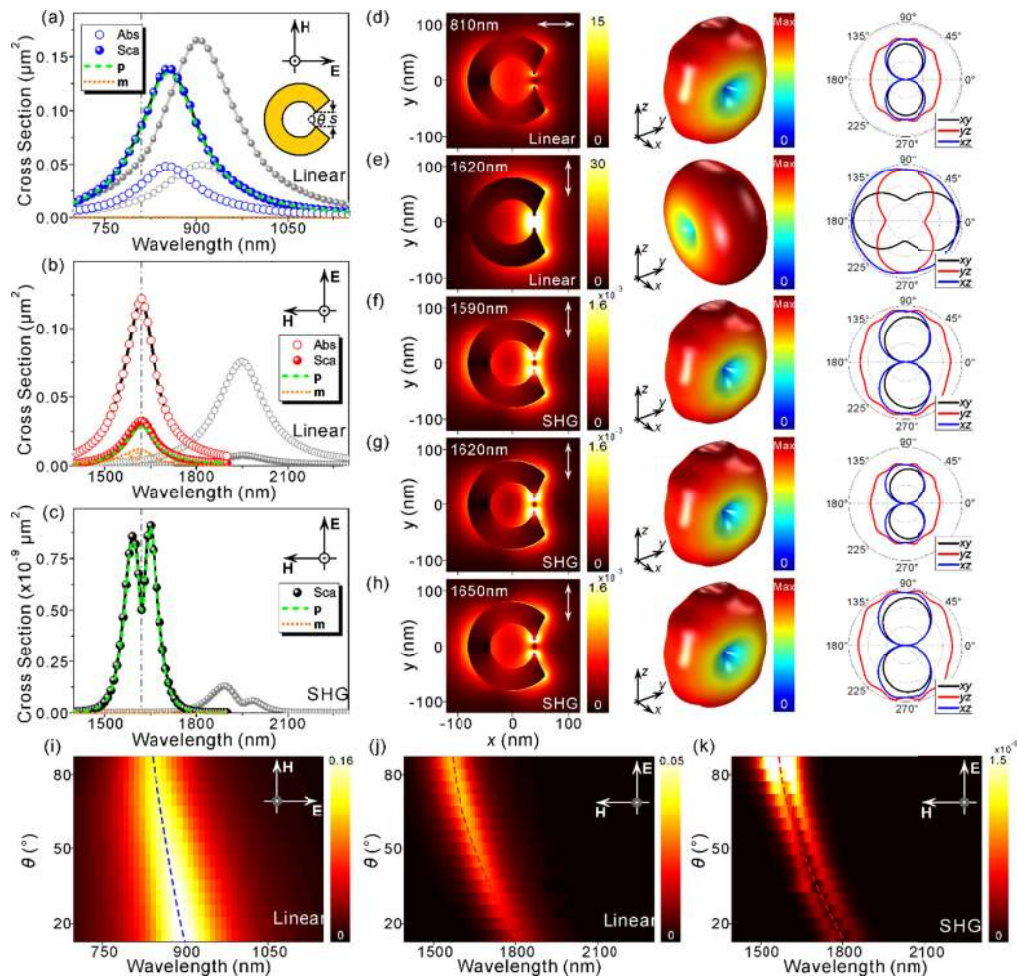


**Fig. 3.** Similar results as Fig. 1 for tailored SRRs of a V-shaped gap. The gap geometry is characterized by the tip-to-tip separation  $s$  and the apex angle  $\theta$  as sketched in the inset of (a). In (a-h),  $R = 80$  nm,  $r = 40$  nm,  $s = 20$  nm,  $\theta = 65^\circ$ ; in (i-k),  $R = 80$  nm,  $r = 40$  nm,  $s = 20$  nm. In (a-c), the gray points show the spectra for a conventional SRR with  $G = 20$  nm and other parameters the same as above.

enhancement caused by the lightning rod effect has been explicitly considered in the numerical calculations.

The variation of the optical responses by adjusting the gap angle  $\theta$  further confirms that the silenced SHG can be effectively restored with the modified SRRs. Figures 3(i) and 3(j) demonstrate, respectively, the linear scattering spectra when the incident polarization is along the  $x$ - and the  $y$ -axis, and the ED and the MD modes blue shift with the increasing of  $\theta$ . At the same time, due to the formation of the sharper apexes, stronger near-field enhancements can be generated with the excitation of the MD mode for the modified SRRs. Although there are strong cancellations of the nonlinear fields around the apex regions, the effective nonlinear sources are enhanced with the present of the oblique surfaces, and the SHG scattering is amplified significantly with the increasing of  $\theta$  (Fig. 3(k)).

Another way to enlarge the SHG is by adjusting the gap separation  $s$ . For the modified SRRs with  $s = 3, 9$  and  $20$  nm, Figs. 4(a) and 4(b) demonstrate, respectively, the linear scattering spectra



for  $x$ - and  $y$ -polarized incidences, and the SHG scattering spectra are presented in Fig. 4(c). To better show the variations, Figs. 4(d) – 4(f) demonstrate the corresponding linear and nonlinear scattering spectra when  $s$  is in the range of 40–3 nm. It is found that the ED mode red shifts slightly with the decreasing of  $s$  (Figs. 4(a) and 4(d)), while the resonance energy is reduced significantly for the MD mode (Figs. 4(b) and 4(e)). When  $s$  is in the range of 40–9 nm, the SHG scattering is enhanced with the reduction of the gap separation. And this observation can be understood from the following two aspects. The first one is that the near-field can be further enhanced when the gap width is reduced, which results in amplified nonlinear sources. The second one is that the MD and the ED modes are approaching to each other for SHG, and the nonlinear scattering can be enhanced by a better spectral mode-matching condition. On the other hand, when  $s$  is in the range of 3–9 nm, the near-field can be further enhanced with the decreasing of the separation (Fig. 8), but the MD and ED modes are mismatched for SHG (Figs. 4(c) and 4(f)). For example, when  $s = 3$  nm, the SHG wavelength is located at the tail of the ED mode (the triangle points, Figs. 4(a) – 4(c)), which means that the nonlinear scattering can only be weakly amplified by the ED mode, and the SHG cross section drops significantly by further decreasing  $s$ . The strongest SHG is optimized at  $s = 9$  nm, where the above mentioned conditions are both fulfilled, the nonlinear sources are relatively strong, and the scattering efficiency can be effectively amplified by the ED mode. The maximum SHG scattering cross section is  $1.31 \times 10^{-9} \mu\text{m}^2$ , and the maximum conversion efficiency is enlarged to  $1.49 \times 10^{-8}$ . It is worthwhile noting that in the above studies, the modified SRRs still possess a mirror symmetry with respect to the horizontal axis. Therefore, partial cancellation of nonlinear fields around the gap region of the modified SRRs still occurs, which can be an obstacle for further SHG enhancement. Previous studies have shown that there are more nonzero susceptibility components for plasmonic structures without mirror symmetry, and thus one can expect to further optimize the SHG efficiency by using SRRs with asymmetric gaps.

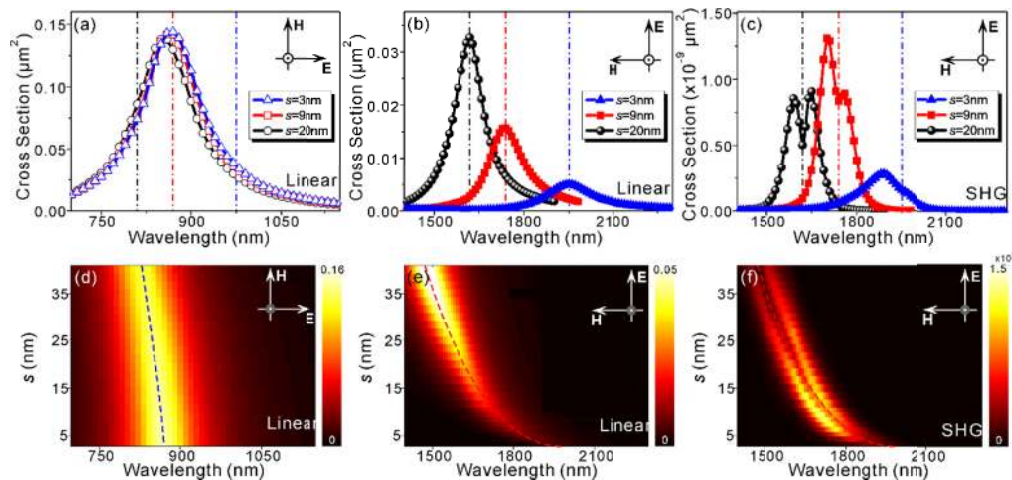


**Fig. 4.** Tuning SHG in tailored SRRs by adjusting the tip-to-tip gap separation  $s$ . Here the SRRs have  $R = 80$  nm,  $r = 40$  nm,  $\theta = 65^\circ$ , and a thickness of 30 nm. (a-c) Fundamental (a, b) and SHG (c) scattering spectra for  $s$ -varied SRR under (a)  $x$ - and (b)  $y$ -polarized incidence. (d-f) Fundamental (d, e) and SHG scattering cross sections as functions of the tip-to-tip gap separation  $s$  and incident wavelength under  $x$ - (d) and  $y$ -polarized incidence (e, f). The blue and red dashed lines denote the spectral positions of the ED and MD modes, respectively.

## 5. Conclusion

In conclusion, this study shows that, owing to the cancelation of nonlinear fields in the gap region, the silenced SHG significantly attenuates the overall nonlinear conversion efficiency of conventional SRRs. We propose and theoretically demonstrate that the silenced SHG can be effectively restored by carefully tailoring the gap geometry, where a better spatial mode overlap between the MD mode at the fundamental wavelength and the ED mode at the SH wavelength can be achieved. The calculation results indicate that the SHG intensity can be more than seven times as large as that of the conventional SRR, and the conversion efficiency can be as large as  $1.49 \times 10^{-8}$  when the outer radius, inner radius and thickness of the SRR are 80, 40 and 30 nm, respectively. These observations indicate that the cancelation of nonlinear fields for SHG can be effectively reduced by tactfully adjusting the shape of plasmonic nanostructures around the hot-spot areas, thus it is of great importance to purposely engineer the geometry of plasmonic nanoparticles to stimulate an enhanced SHG. It is expected that SHG intensities and conversion efficiencies can be further enhanced when the structure is hybridized with nanoparticles composed of conventional nonlinear materials. Besides that, the ideal ED scattering characteristic for SHG is maintained with the modified SRRs, which is very useful for nonlinear far-field manipulation such as beam steering and holograms.

## Appendix A: Additional near- and far-field distributions for SRRs

The near-field enhancement factor in a plasmonic nanostructure can be enlarged when the incidence frequency is approaching to the LSPR of the system. Therefore, one can get the strongest near-field enhancements when the incidence matches with the MD mode for the conventional SRR with  $G = 30$  nm ( $\lambda_{\text{inc}} = 1800$  nm, Fig. 5). Since the intensity of the nonlinear source is proportional to the field intensity at the fundamental wavelength, the generated nonlinear source is the strongest around the MD mode. However, the SHG scattering is attenuated caused by the silenced SHG (Fig. 1).

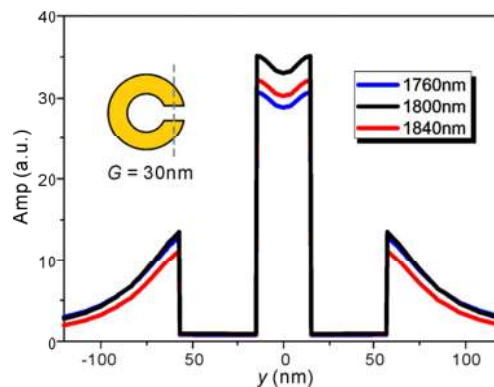


**Fig. 5.** The amplitude of the electric field distributions along the dashed line of the conventional SRR for the MD mode, where the geometry parameters and excitation conditions are identical with that of Fig. 1(b).

Figure 6 demonstrates the near- and far-field distributions for the conventional SRR with  $G = 20$  nm. The near-field enhancements around the gap area are indeed further enlarged compared with that of  $G = 30$  nm (Fig. 7), thereby leading to stronger nonlinear sources. However, the cancelation of nonlinear fields would be more effective in this case, and the SHG emission intensity is weaker than that of  $G = 30$  nm (Fig. 1(k)).

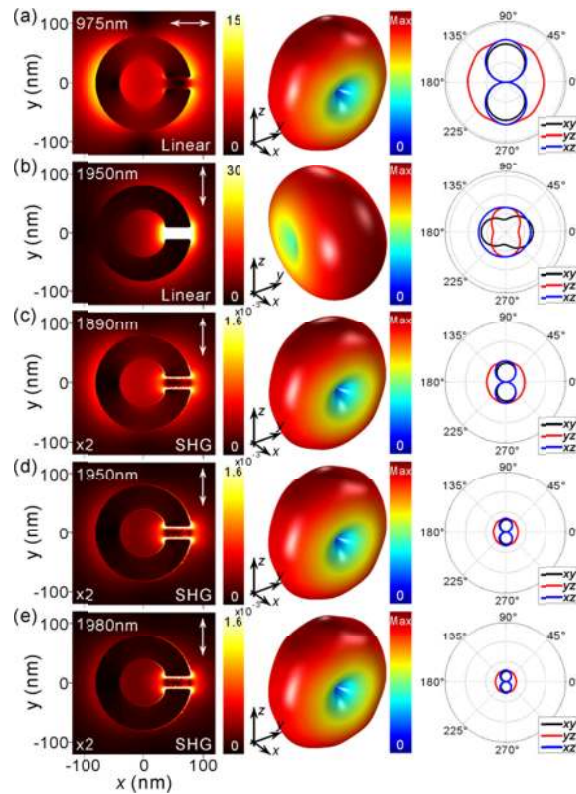


**Fig. 6.** The amplitude of near-field distributions (the left panels), the three dimensional far-field scattering patterns (the middle panels), and the cross section views of the far-field scattering patterns with  $x$ -polarized incidence and  $\lambda_{\text{inc}} = 975 \text{ nm}$  (a),  $y$ -polarized incidence and  $\lambda_{\text{inc}} = 1950 \text{ nm}$  (b), and SHG of the SRR with  $y$ -polarized incidence and  $\lambda_{\text{inc}} = 1890 \text{ nm}$  (c),  $1950 \text{ nm}$  (d), and  $1980 \text{ nm}$  (e), where the SHG near-field distributions have been scaled by a factor of 2, the gap width  $G = 20 \text{ nm}$ , and the rest geometry parameters for the conventional SRR are identical with that of Fig. 1.

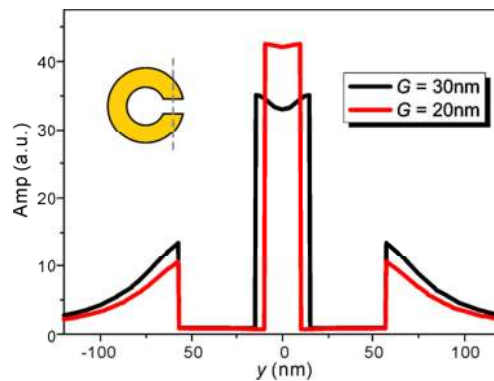


**Fig. 7.** The amplitude of the electric field distributions along the dashed line of the conventional SRR for the MD mode when the gap width  $G = 30 \text{ nm}$  (the black line) and  $20 \text{ nm}$  (the red line), where the rest geometry parameters are identical with that of Fig. 1.

For the modified SRR with  $s = 3$  nm, the stronger plasmon interaction around the gap region results in stronger near-field enhancements compared with that of  $s = 9$  nm (Figs. 8(a) – 8(c)). Therefore, the nonlinear sources for the SRR with  $s = 3$  nm would be stronger than that of  $s = 9$  nm. However, the cancelation of nonlinear fields would be more effective for  $s = 3$  nm. In addition, the MD mode mismatches with the ED mode for SHG, and the SHG scattering decreases for the modified SRR with a narrower gap width (Figs. 8(d) – 8(f)).

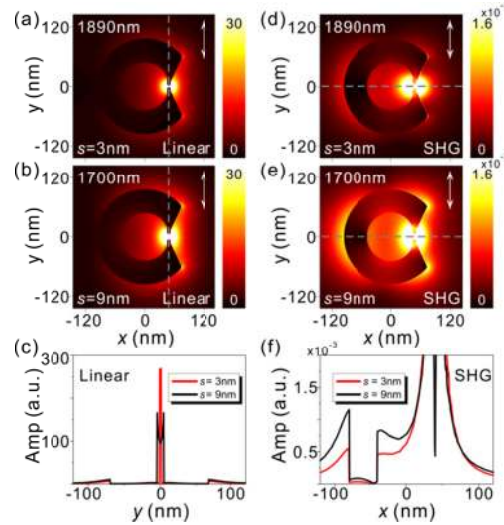


**Fig. 8.** (a) Near-field distributions of the MD mode for the modified SRRs with  $s = 3$  nm and (b) 9 nm. (c) The comparison of the amplitude of the electric field distributions along the dashed line of the modified SRRs with different gap separations. (d-f) The corresponding SHG near-field distributions. The rest geometry parameters of the SRRs are identical with that of Fig. 3.

## Appendix B: Electromagnetic simulation and multipolar decompositions

Finite element method was used to calculate the linear and the nonlinear optical responses of the SRRs, where the measured complex dielectric constants of gold were used in the calculations [60]. For simplicity but without loss of generality, the refractive index of the surrounding medium is supposed to be 1.25. In the simulations, the structure corners are rounded by 3 nm to avoid unphysical singularities. The linear scattering responses of the SRRs at the fundamental wavelength with a  $y$ -polarized incidence were calculated at first, and one can get the linear spectra and the fundamental near-field distributions. Then, the nonlinear sources are calculated based on the fundamental near-field distributions. After that, the linear scattering responses of the SRRs at the SHG wavelength were calculated by using the nonlinear sources derived from the second step. From the hydrodynamic model, the nonlinear source for SHG can be written as [52],

$$\mathbf{S}_{NL} = \frac{e}{m_e^*} \mathbf{E}_1 (\nabla \cdot \mathbf{P}_1) + \frac{i\omega e}{m_e^*} \mathbf{P}_1 \times \mathbf{B}_1 - \frac{\omega^2}{n_0 e} [(\nabla \cdot \mathbf{P}_1) \mathbf{P}_1 + (\mathbf{P}_1 \cdot \nabla) \mathbf{P}_1] \quad (1)$$

where  $n_0 = 5.7 \times 10^{22} \text{ cm}^{-3}$  is the equilibrium charge density,  $m_e^*$  denotes the effective electron mass, the subscript “1” refer to the fundamental fields, and the three parts on the right side denote the nonlinear Coulomb term, the magnetic Lorentz force contribution, and the convective terms, respectively. One can get an accurate description of SHG with the above nonlinear source, but the resolution of nonlocal equations is required, and the simulation is hard to implement caused

by considerable computational resources. Since the electron pressure term in the bulk region can be neglected, the nonlinear surface polarization can be written as,

$$\mathbf{P}_2^S = -\frac{1}{2n_0e}[(\nabla \cdot \mathbf{P}_1)\mathbf{P}_1 + \frac{\omega}{2\omega + i\gamma}(\mathbf{P}_1 \cdot \nabla)\mathbf{P}_1] \quad (2)$$

Then, the effective nonlinear surface current density is given by,

$$\mathbf{K}_{NL} = \frac{i\omega}{n_0e} \left[ \hat{\mathbf{t}}(P_1^\perp P_1^\parallel) + \hat{\mathbf{n}} \frac{1}{2} \frac{3\omega + i\gamma}{2\omega + i\gamma} (P_1^\perp)^2 \right] \quad (3)$$

Where  $\mathbf{K}_{NL} = 2i\omega \int \mathbf{P}_2^S(\mathbf{r})d\mathbf{r}$  is used, the integral is performed across the surface layer,  $\hat{\mathbf{n}}$  is a unit vector perpendicular to the surface of the structure, the unit vector  $\hat{\mathbf{t}}$  pointing in the direction  $\hat{\mathbf{n}} \times \mathbf{P}_2^S$ , and  $\gamma = 1.07 \times 10^{14} \text{ s}^{-1}$  is the electron collision rate. The effective nonlinear surface current density is related to the polarization values in the bulk region and do not require the resolution of nonlocal equations, which makes it possible to study SHG with full three-dimensional simulations. In this way, the SHG scattering cross sections can be quantitatively determined, and the SHG conversion efficiency can be defined as the ratio between the SHG scattering and the fundamental extinction cross sections. In the hydrodynamic model, the effective SH surface currents in terms of polarization vector in the bulk region of a metal nanostructure have been used as the sources to calculate its nonlinear responses. Therefore, it can be used to study SHG in metallic nanoparticles of arbitrary shapes. As for the plasmonic SRR studied here, the excitation of its MD mode at the fundamental wavelength leads to strong effective SH surface currents (nonlinear sources) around the tiny gap area, while the ED mode at the SH wavelength results in an amplification of its SHG scattering efficiency. Both aspects have been fully considered in our numerical calculations. Previous studies have shown that the calculated SHG results for small SRRs using the hydrodynamic model agree qualitatively well with the experimental data [52]. It is however worthwhile noting that the electron pressure term in the bulk region has been neglected in the hydrodynamic model. As a result, for metallic nanoparticles with a very thin thickness or a very tiny gap (*e.g.*,  $\sim 1 \text{ nm}$ ), the electron pressure term in the bulk region should be considered to obtain more accurate SHG results.

The Cartesian multipole decomposition can be calculated with the induced polarization inside the SRRs [61],

$$\mathbf{P} = \varepsilon_0(\varepsilon_p - \varepsilon_d)\mathbf{E} \quad (4)$$

where  $\varepsilon_0$ ,  $\varepsilon_d$  and  $\varepsilon_p$  denote the vacuum dielectric constant, the relative dielectric permittivity of the surrounding medium, and the relative dielectric permittivity of the SRRs, respectively. The total electric field ( $\mathbf{E}$ ) inside the SRRs can be evaluated with the numerical calculations. To get the Cartesian multipole expansion of the light-induced polarization,

$$\mathbf{P}(\mathbf{r}) = \int \mathbf{P}(\mathbf{r}')\delta(\mathbf{r} - \mathbf{r}')d\mathbf{r}' \quad (5)$$

the Dirac delta function  $\delta(\mathbf{r} - \mathbf{r}')$  is expanded in a Taylor series with respect to  $\mathbf{r}'$  around the origin. Then one can get the irreducible representations for the Cartesian electric dipole and toroidal dipole,

$$\mathbf{p} = \int \mathbf{P}(\mathbf{r}')d\mathbf{r}' \quad (6)$$

$$\mathbf{T} = \frac{i\omega}{10} \int \{2\mathbf{r}'^2\mathbf{P}(\mathbf{r}') - [\mathbf{r}' \cdot \mathbf{P}(\mathbf{r}')] \mathbf{r}'\}d\mathbf{r}' \quad (7)$$

the magnetic dipole,

$$\mathbf{m} = -\frac{i\omega}{2} \int [\mathbf{r}' \times \mathbf{P}(\mathbf{r}')]d\mathbf{r}' \quad (8)$$

Then, the total scattering power by considering the dipole contributions can be calculated by [61],

$$P_{\text{sca}} = \frac{k_0^4}{12\pi\epsilon_0^2 v_d \mu_0} \left| \mathbf{p} + \frac{ik_d}{v_d} \mathbf{T} \right|^2 + \frac{k_0^4 \epsilon_d}{12\pi\epsilon_0 v_d} |\mathbf{m}|^2 \quad (9)$$

where the first and second terms are the total ED and MD contributions, respectively.

## Funding

National Natural Science Foundation of China (11574228, 11874276); Hong Kong Research Grants Council (GRF 15303417); San Jin Scholars Program of Shanxi Province.

## Acknowledgments

The authors acknowledge useful discussions with Dr. Meng Qiu at The Hong Kong Polytechnic University.

## References

1. J. Butet, P. F. Brevet, and O. J. F. Martin, "Optical second harmonic generation in plasmonic nanostructures: From fundamental principles to advanced applications," *ACS Nano* **9**(11), 10545–10562 (2015).
2. M. Kauranen and A. V. Zayats, "Nonlinear plasmonics," *Nat. Photonics* **6**(11), 737–748 (2012).
3. F. Timpu, J. Sendra, C. Renaud, L. Lang, M. Timofeeva, M. T. Buscaglia, V. Buscaglia, and R. Grange, "Lithium niobate nanocubes as linear and nonlinear ultraviolet Mie resonators," *ACS Photonics* **6**(2), 545–552 (2019).
4. J. Butet, J. Duboisset, G. Bachelier, I. Russier-Antoine, E. Benichou, C. Jonin, and P. F. Brevet, "Optical second harmonic generation of single metallic nanoparticles embedded in a homogeneous medium," *Nano Lett.* **10**(5), 1717–1721 (2010).
5. J. Butet, G. Bachelier, I. Russier-Antoine, C. Jonin, E. Benichou, and P.-F. Brevet, "Interference between selected dipoles and octupoles in the optical second-harmonic generation from spherical gold nanoparticle," *Phys. Rev. Lett.* **105**(7), 077401 (2010).
6. Y. Zhang, N. K. Grady, C. Ayala-Orozco, and N. J. Halas, "Three-dimensional nanostructures as highly efficient generators of second harmonic light," *Nano Lett.* **11**(12), 5519–5523 (2011).
7. H. Aouani, M. Navarro-Cia, M. Rahmani, T. P. H. Sidiropoulos, M. H. Hong, R. F. Oulton, and S. A. Maier, "Multiresonant broadband optical antennas as efficient tunable nanosources of second harmonic light," *Nano Lett.* **12**(9), 4997–5002 (2012).
8. Q. Ai, L. L. Gui, D. Paone, B. Metzger, M. Mayer, K. Weber, A. Fery, and H. Giessen, "Ultrannarrow second-harmonic resonances in hybrid plasmon-fiber cavities," *Nano Lett.* **18**(9), 5576–5582 (2018).
9. A. Gomez-Tornero, C. Tserkezis, J. R. Moreno, L. E. Bausa, and M. O. Ramirez, "Field enhancement and spectral features of hexagonal necklaces of silver nanoparticles for enhanced nonlinear optical processes," *Opt. Express* **26**(17), 22394–22404 (2018).
10. S. V. Makarov, M. I. Petrov, U. Zywiets, V. Milichko, D. Zuev, N. Lopanitsyna, A. Kuksin, I. Mukhin, G. Zograf, E. Ubyivovk, D. A. Smirnova, S. Starikov, B. N. Chichkov, and Y. S. Kivshar, "Efficient second-harmonic generation in nanocrystalline silicon nanoparticles," *Nano Lett.* **17**(5), 3047–3053 (2017).
11. J. Butet and O. J. F. Martin, "Nonlinear plasmonic nanorulers," *ACS Nano* **8**(5), 4931–4939 (2014).
12. J. Butet and O. J. F. Martin, "Refractive index sensing with Fano resonant plasmonic nanostructures: a symmetry based nonlinear approach," *Nanoscale* **6**(24), 15262–15270 (2014).
13. J. Butet, I. Russier-Antoine, C. Jonin, N. Lascoux, E. Benichou, and P. F. Brevet, "Sensing with multipolar second harmonic generation from spherical metallic nanoparticles," *Nano Lett.* **12**(3), 1697–1701 (2012).
14. S. X. Shen, L. Y. Meng, Y. J. Zhang, J. B. Han, Z. W. Ma, S. Hu, Y. H. He, J. F. Li, B. Ren, T. M. Shih, Z. H. Wang, Z. L. Yang, and Z. Q. Tian, "Plasmon-enhanced second-harmonic generation nanorulers with ultrahigh sensitivities," *Nano Lett.* **15**(10), 6716–6721 (2015).
15. J. Butet, K. Thyagarajan, and O. J. F. Martin, "Ultrasensitive optical shape characterization of gold nanoantennas using second harmonic generation," *Nano Lett.* **13**(4), 1787–1792 (2013).
16. G. Li, S. Zhang, and T. Zentgraf, "Nonlinear photonic metasurfaces," *Nat. Rev. Mater.* **2**(5), 17010 (2017).
17. N. Segal, S. Keren-Zur, N. Hendler, and T. Ellenbogen, "Controlling light with metamaterial-based nonlinear photonic crystals," *Nat. Photonics* **9**(3), 180–184 (2015).
18. M. Tymchenko, J. S. Gomez-Diaz, J. Lee, N. Nookala, M. A. Belkin, and A. Alu, "Gradient nonlinear Pancharatnam-Berry metasurfaces," *Phys. Rev. Lett.* **115**(20), 207403 (2015).
19. S. Keren-Zur, O. Avayu, L. Michaeli, and T. Ellenbogen, "Nonlinear beam shaping with plasmonic metasurfaces," *ACS Photonics* **3**(1), 117–123 (2016).
20. G. X. Li, S. M. Chen, N. Pholchai, B. Reineke, P. W. H. Wong, E. Y. B. Pun, K. W. Cheah, T. Zentgraf, and S. Zhang, "Continuous control of the nonlinearity phase for harmonic generations," *Nat. Mater.* **14**(6), 607–612 (2015).

21. W. M. Ye, F. Zeuner, X. Li, B. Reineke, S. He, C. W. Qiu, J. Liu, Y. T. Wang, S. Zhang, and T. Zentgraf, "Spin and wavelength multiplexed nonlinear metasurface holography," *Nat. Commun.* **7**(1), 11930 (2016).
22. G. X. Li, L. Wu, K. F. Li, S. M. Chen, C. Schlickriede, Z. J. Xu, S. Y. Huang, W. D. Li, Y. J. Liu, E. Y. B. Pun, T. Zentgraf, K. W. Cheah, Y. Luo, and S. Zhang, "Nonlinear metasurface for simultaneous control of spin and orbital angular momentum in second harmonic generation," *Nano Lett.* **17**(12), 7974–7979 (2017).
23. G. Bautista, M. J. Huttunen, J. Makitalo, J. M. Kontio, J. Simonen, and M. Kauranen, "Second-harmonic generation imaging of metal nano-objects with cylindrical vector beams," *Nano Lett.* **12**(6), 3207–3212 (2012).
24. F. Walter, G. X. Li, C. Meier, S. Zhang, and T. Zentgraf, "Ultrathin nonlinear metasurface for optical image encoding," *Nano Lett.* **17**(5), 3171–3175 (2017).
25. T. Xu, X. Jiao, G. P. Zhang, and S. Blair, "Second-harmonic emission from sub-wavelength apertures: Effects of aperture symmetry and lattice arrangement," *Opt. Express* **15**(21), 13894–13906 (2007).
26. B. K. Canfield, H. Husu, J. Laukkanen, B. F. Bai, M. Kuittinen, J. Turunen, and M. Kauranen, "Local field asymmetry drives second-harmonic generation in noncentrosymmetric nanodimers," *Nano Lett.* **7**(5), 1251–1255 (2007).
27. L. Michaeli, S. Keren-Zur, O. Avayu, H. Suchowski, and T. Ellenbogen, "Nonlinear surface lattice resonance in plasmonic nanoparticle arrays," *Phys. Rev. Lett.* **118**(24), 243904 (2017).
28. R. Czaplicki, A. Kiviniemi, M. J. Huttunen, X. Zang, T. Stolt, I. Vartiainen, J. Butet, M. Kuittinen, O. J. F. Martin, and M. Kauranen, "Less is more: Enhancement of second-harmonic generation from metasurfaces by reduced nanoparticle density," *Nano Lett.* **18**(12), 7709–7714 (2018).
29. D. C. Hooper, C. Kuppe, D. Wang, W. Wang, J. Guan, T. W. Odom, and V. K. Valev, "Second harmonic spectroscopy of surface lattice resonances," *Nano Lett.* **19**(1), 165–172 (2019).
30. K. Thyagarajan, J. Butet, and O. J. F. Martin, "Augmenting second harmonic generation using Fano resonances in plasmonic systems," *Nano Lett.* **13**(4), 1847–1851 (2013).
31. S. D. Liu, E. S. P. Leong, G. C. Li, Y. D. Hou, J. Deng, J. H. Teng, H. C. Ong, and D. Y. Lei, "Polarization-independent multiple Fano resonances in plasmonic nonamers for multimode-matching enhanced multiband second-harmonic generation," *ACS Nano* **10**(1), 1442–1453 (2016).
32. S. Zhang, G. C. Li, Y. Q. Chen, X. P. Zhu, S. D. Liu, D. Y. Lei, and H. G. Duan, "Pronounced Fano resonance in single gold split nanodisks with 15 nm split gaps for intensive second harmonic generation," *ACS Nano* **10**(12), 11105–11114 (2016).
33. D. J. Yang, S. J. Im, G. M. Pan, S. J. Ding, Z. J. Yang, Z. H. Hao, L. Zhou, and Q. Q. Wang, "Magnetic Fano resonance-induced second-harmonic generation enhancement in plasmonic metamolecule rings," *Nanoscale* **9**(18), 6068–6075 (2017).
34. B. Metzger, L. L. Gui, J. Fuchs, D. Floess, M. Hentschel, and H. Giessen, "Strong enhancement of second harmonic emission by plasmonic resonances at the second harmonic wavelength," *Nano Lett.* **15**(6), 3917–3922 (2015).
35. M. Celebrano, X. F. Wu, M. Baselli, S. Grossmann, P. Biagioni, A. Locatelli, C. De Angelis, G. Cerullo, R. Osellame, B. Hecht, L. Duo, F. Ciccacci, and M. Finazzi, "Mode matching in multiresonant plasmonic nanoantennas for enhanced second harmonic generation," *Nat. Nanotechnol.* **10**(5), 412–417 (2015).
36. G. Grinblat, M. Rahmani, E. Cortes, M. Caldarola, D. Comedi, S. A. Maier, and A. V. Bragas, "High-efficiency second harmonic generation from a single hybrid ZnO nanowire/Au plasmonic nano-oligomer," *Nano Lett.* **14**(11), 6660–6665 (2014).
37. D. Lehr, J. Reinhold, I. Thiele, H. Hartung, K. Dietrich, C. Menzel, T. Pertsch, E. B. Kley, and A. Tunnermann, "Enhancing second harmonic generation in gold nanoring resonators filled with lithium niobate," *Nano Lett.* **15**(2), 1025–1030 (2015).
38. F. Timpu, N. R. Hendricks, M. Petrov, S. B. Ni, C. Renaut, H. Wolf, L. Isa, Y. Kivshar, and R. Grange, "Enhanced second-harmonic generation from sequential capillarity-assisted particle assembly of hybrid nanodimers," *Nano Lett.* **17**(9), 5381–5388 (2017).
39. Y. Li, M. Kang, J. J. Shi, K. Wu, S. P. Zhang, and H. Xu, "Transversely divergent second harmonic generation by surface plasmon polaritons on single metallic nanowires," *Nano Lett.* **17**(12), 7803–7808 (2017).
40. B. N. Carnio and A. Y. Elezzabi, "Second harmonic generation in metal-LiNbO<sub>3</sub>-metal and LiNbO<sub>3</sub> hybrid-plasmonic waveguides," *Opt. Express* **26**(20), 26283–26291 (2018).
41. J. Berthelot, G. Bachelier, M. X. Song, P. Rai, G. C. des Francs, A. Dereux, and A. Bouhelier, "Silencing and enhancement of second-harmonic generation in optical gap antennas," *Opt. Express* **20**(10), 10498–10508 (2012).
42. A. Slablab, L. Le Xuan, M. Zielinski, Y. de Wilde, V. Jacques, D. Chauvat, and J. F. Roch, "Second-harmonic generation from coupled plasmon modes in a single dimer of gold nanospheres," *Opt. Express* **20**(1), 220–227 (2012).
43. L. J. Black, P. R. Wiecha, Y. D. Wang, C. H. de Groot, V. Paillard, C. Girard, O. L. Muskens, and A. Arbouet, "Tailoring second harmonic generation in single L-shaped plasmonic nanoantennas from the capacitive to conductive coupling regime," *ACS Photonics* **2**(11), 1592–1601 (2015).
44. G. Bautista, C. Dreser, X. R. Zang, D. P. Kern, M. Kauranen, and M. Fleischer, "Collective effects in second-harmonic generation from plasmonic oligomers," *Nano Lett.* **18**(4), 2571–2580 (2018).
45. G. Sartorello, N. Olivier, J. J. Zhang, W. S. Yue, D. J. Gosztola, G. P. Wiederrecht, G. Wurtz, and A. V. Zayats, "Ultrafast optical modulation of second- and third-harmonic generation from cut-disk-based metasurfaces," *ACS Photonics* **3**(8), 1517–1522 (2016).
46. D. de Ceglia, M. A. Vincenti, C. de Angelis, A. Locatelli, J. W. Haus, and M. Scalora, "Role of antenna modes and field enhancement in second harmonic generation from dipole nanoantenna," *Opt. Express* **23**(2), 1715–1729 (2015).

47. K. Thyagarajan, S. Rivier, A. Lovera, and O. J. F. Martin, "Enhanced second-harmonic generation from double resonant plasmonic antennae," *Opt. Express* **20**(12), 12860–12865 (2012).
48. J. Butet, G. D. Bernasconi, M. Petit, A. Bouhelier, C. Yan, O. J. F. Martin, B. Cluzel, and O. Demichel, "Revealing a mode interplay that controls second-harmonic radiation in gold nanoantennas," *ACS Photonics* **4**(11), 2923–2929 (2017).
49. R. Sanatinia, S. Anand, and M. Swillo, "Modal engineering of second-harmonic generation in single GaP nanopillars," *Nano Lett.* **14**(9), 5376–5381 (2014).
50. C. Renaut, L. Lang, K. Frizyuk, M. Timofeeva, F. E. Komissarenko, I. S. Mukhin, D. Smirnova, F. Timpu, M. Petrov, Y. Kivshar, and R. Grange, "Reshaping the second-order polar response of hybrid metal-dielectric nanodimers," *Nano Lett.* **19**(2), 877–884 (2019).
51. M. W. Klein, C. Enkrich, M. Wegener, and S. Linden, "Second-harmonic generation from magnetic metamaterials," *Science* **313**(5786), 502–504 (2006).
52. C. Ciraci, E. Poutrina, M. Scalora, and D. R. Smith, "Origin of second-harmonic generation enhancement in optical split-ring resonators," *Phys. Rev. B* **85**(20), 201403 (2012).
53. S. Linden, F. B. P. Niesler, J. Förstner, Y. Grynko, T. Meier, and M. Wegener, "Collective effects in second-harmonic generation from split-ring-resonator arrays," *Phys. Rev. Lett.* **109**(1), 015502 (2012).
54. W. Y. Tsai, T. L. Chung, H. H. Hsiao, J. W. Chen, R. J. Lin, P. C. Wu, G. Sun, C. M. Wang, H. Misawa, and D. P. Tsai, "Second harmonic light manipulation with vertical split ring resonators," *Adv. Mater.* **31**, 1806479 (2018).
55. F. X. Wang, F. J. Rodriguez, W. M. Albers, R. Ahorinta, J. E. Sipe, and M. Kauranen, "Surface and bulk contributions to the second-order nonlinear optical response of a gold film," *Phys. Rev. B* **80**(23), 233402 (2009).
56. G. Bachelier, J. Butet, I. Russier-Antoine, C. Jonin, E. Benichou, and P.-F. Brevet, "Origin of optical second-harmonic generation in spherical gold nanoparticles: Local surface and nonlocal bulk contributions," *Phys. Rev. B* **82**(23), 235403 (2010).
57. C. Ciraci, E. Poutrina, M. Scalora, and D. R. Smith, "Second-harmonic generation in metallic nanoparticles: Clarification of the role of the surface," *Phys. Rev. B* **86**(11), 115451 (2012).
58. G. D. Bernasconi, J. Butet, and O. J. F. Martin, "Dynamics of second-harmonic generation in a plasmonic silver nanorod," *ACS Photonics* **5**(8), 3246–3254 (2018).
59. O. A. Aktsipetrov, I. M. Baranova, E. D. Mishina, and A. V. Petukhov, "Lightning rod effect in surface-enhanced second harmonic generation," *JETP Lett.* **40**, 1012–1015 (1984).
60. P. B. Johnson and R. W. Christy, "Optical constants of the noble metals," *Phys. Rev. B* **6**(12), 4370–4379 (1972).
61. A. B. Evlyukhin, T. Fischer, C. Reinhardt, and B. N. Chichkov, "Optical theorem and multipole scattering of light by arbitrarily shaped nanoparticles," *Phys. Rev. B* **94**(20), 205434 (2016).